Received June 9, 2020, accepted July 1, 2020, date of publication July 6, 2020, date of current version July 20, 2020.

Digital Object Identifier 10.1109/ACCESS.2020.3007576

High-Gain, Circularly-Polarized THz Antenna With Proper Modeling of Structures With Thin Metallic Walls

DOMINIKA WARMOWSKA[1], KERLOS ATIA ABDALMALAK[2,3], (Graduate Student Member, IEEE), LUIS ENRIQUE GARCÍA MUÑOZ[2], AND ZBYNEK RAIDA[1], (Senior Member, IEEE)

[1]Department of Radio Electronics, Faculty of Electrical Engineering and Communication, Brno University of Technology, 601 90 Brno, Czech Republic
[2]Department of Signal Theory and Communications, Carlos III University of Madrid, 28903 Getafe, Spain
[3]Department of Electrical Engineering, Aswan University, Aswan 81542, Egypt

Corresponding author: Dominika Warmowska (dominika.warmowska@gmail.com)

This work was supported in part by the Innovative Training Network Convergence of Electronics and Photonics Technologies for Enabling Terahertz Applications (ITN CELTA) through the H2020 under Grant 675683, in part by the CEITEC Nano Research Infrastructure through the Ministry of Education, Youth and Sport of the Czech Republic (MEYS CR) under Grant LM2018110, and in part by Comunidad de Madrid MARTINLARA Project under Grant P2018/NMT-4333.

ABSTRACT In the paper, a corporate feed antenna array with slot radiators and a layer of polarizing patches is designed to operate at 350 GHz. The antenna is conceived as a silicon structure fully metalized by gold. Different methods for modeling thin gold layers at terahertz frequencies are compared and the optimum approaches are chosen depending on the thickness of the metal layer and its relation to the skin depth. Two designed antenna arrays are in 2×2 and 4×4 configuration, radiate circularly polarized waves, and have high gains of 13.8 dBic and 18.4 dBic, respectively. Antenna arrays have a low profile of only 1.3 λ_0. Cheaper and more available manufacturing technology is presented and discussed in detail together with the measurement results of three manufactured prototypes. Small deviations between the simulated results and the measured ones are obtained due to a lower surface roughness, which is confirmed by the scanning probe microscope. Comparison with state-of-the-art antenna arrays demonstrates that the proposed arrays excel in easy/low-cost manufacturing, high gain, circular polarization with good axial-ratio bandwidth, compact size, and the possibility to easily extend the array into a larger version.

INDEX TERMS Antenna nanofabrication, high-gain, low-profile, terahertz antenna array, terahertz gold conductivity, terahertz metal characterization, thin gold modeling.

I. INTRODUCTION

Electromagnetic waves at THz frequencies provide a solution to increasing demands on a wider bandwidth and higher data rates, which enables to operate many applications in communication systems on the Earth or in satellite systems. Moreover, THz waves exhibit different penetration characteristics than other frequency bands, which is beneficial for applications in security and medical imaging. Another application for systems operating in the terahertz frequency is space observation. Therefore, millimeter-wave antennas have been extensively researched in the last decades [1], [2].

While more information can be sent faster in the THz range, the free-space loss and wave absorption is higher for those waves. Hence, high-gain antennas are necessary to overcome those high path losses. To eliminate the necessity of alignment of communication terminals and lower the losses in case of misalignment, circular polarization is preferred for most communication systems with mobile terminals.

There are many designs of high-gain, circularly polarized antennas in the mm-wave bands. One of the solutions is the Fabry-Perot antenna [3]–[5]. This antenna can radiate circularly polarized waves, has a low profile, and achieves a high gain. However, its bandwidth is very limited (1 to 3%), and its design is proven to be problematic when scaling to THz frequencies, mostly due to fabrication limitations.

At THz frequencies, high-gain, wide bandwidth and circular polarization of the radiated wave can be achieved by spiral antennas. But necessarily, radiation characteristics have to be converted to unidirectional ones which can be performed

The associate editor coordinating the review of this manuscript and approving it for publication was Kuang Zhang.

using two techniques. When using cavities/absorbers, losses are significantly increased [6]. When using conical shapes, fabrication processes can be very tricky and costly. According to the best authors' knowledge, the highest frequency obtained by an actually manufactured porotype is 14 GHz [7].

Lens antennas can overcome the previous challenges by placing a spiral (or other planar antennas) on a dielectric lens, however, these lenses should be electrically large in order of $10\lambda_0$ [8].

Horn antennas are well-known designs. While achieving excellent gains and bandwidths, heights are very large [2]. Similarly, dielectric rod waveguide THz antennas can achieve high gain, but have electrically large height [9]–[12]. The large size of the lens, horn, and dielectric rod antennas can complicate the antenna integrating into modern communication systems. Therefore, a design with a compact geometry, a high gain and circularly polarized radiation with a straightforward manufacturing process is necessary.

On the other hand, corporate feed antennas can be integrated into the system easily. Low-profile, small electrical size, high-gain with the possibility to increase it further by expanding the array and a straight-forward design are further advantages.

Hence, this work presents a THz antenna consisting of multiple thin-layer structures to provide all the mentioned attractive characteristics in a single design.

Modern microfabrication technologies usually allow highly precise manufacturing of devices to be operated up to 100 GHz. At higher frequencies, the microfabrication becomes challenging due to smaller dimensions of devices and the requested very high accuracy.

The nanofabrication allows to manufacture very precise elements for optical frequencies, but some THz designs can be proven to be too large for this technology. In [13], authors presented a multilayered 2×2 antenna array (which played the role of a single antenna element) and a 4×4 array (which was considered to be a 2×2 array). The antennas were designed and manufactured to operate at 1 THz. One of the manufacturing steps included a spin coating by a photoresist of the thickness of $\lambda/4$, which is very thick at lower frequencies, and therefore problematic to manufacture. The presented design is compact and wideband, however, the gain is limited to 10 dBi (the 2×2 array) and 14 dBi (the 4×4 array). Moreover, the antennas do not provide circular polarization.

In [14], the authors presented a larger array with a similar design to be operated at 350 GHz. Also, a silicon-based manufacturing process was included, and the antenna achieved a higher gain. However, the antenna [14] was again designed for linear polarization and had an electrically large height. Another antenna with slot radiators and corporate feed was presented in [15]. It operates at 60 GHz and, although, it is high-gain and circularly polarized, the bandwidth is only 4% and, the design with multiple thin layers is not feasible on THz.

There are very few works available, which present detailed steps of microfabrication of a metalized silicon antenna at THz frequencies. In those few available works, expensive machines (vacuum bonders and deep reactive ion etching machines) are usually used. In this work, we discuss the cost-efficient manufacturing steps of implementing the THz metalized silicon antenna array in detail.

When designing the antenna, a full-wave model has to be developed and optimized. So far, relevant models have been developed for graphene-dielectric substrate integrated waveguides [16] and large-format imaging systems [17]. In case of antennas, attention was dominantly turned to photoconductive elements [18] and arrays [19]. Nevertheless, papers on proper modeling of THz antennas with thin metallic layers are rare.

Simulations of accurate numerical models of THz antennas are CPU-time and memory demanding. In order to optimize such structures, exploitation of the space-mapping technique [20] might be an option. In that approach, a CPU-time and memory modest model of a limited accuracy is used during the optimization routine. In this work, models with limited accuracy and highly precise ones are presented and compared, for different commercially available solvers.

Upscaling millimeter-wave systems to terahertz frequencies requires a proper characterization of used materials (metal conductors and dielectric layers in case of passive components). In the terahertz region, dielectric permittivity and electric conductivity of metallic materials varies with frequency [21], [22]. Those frequency variations have to be carefully incorporated into precise numerical models of passive terahertz structures. A proper way of modeling has to be selected to achieve appropriate results. There are many commercial solvers available and each of them has several different methods that can be used to model a thin metallic layer. In this paper, we present the suitable method based on the relation of the skin depth to the layer thickness.

In [14], an effective value of gold conductivity at 350 GHz was given, based on measurements and approximations of a manufactured cavity. Yet still, there is not much information in the literature about the effects of different nanofabrication steps, during manufacture, on the THz conductivity of gold layers of THz devices. In this work, we present the effects of some nanofabrication steps on the surface roughness and therefore conductivity of a THz antenna.

The paper presents a method for modeling thin gold layers at THz frequencies, a cost-efficient manufacturing method and the design of an antenna with advantageous parameters to be used in THz communications systems.

The paper is organized as follows. Section II discusses the selection of a proper solver and proper boundary conditions for efficient modeling of thin metal THz antennas, depending on the thickness of the gold layer in the structure. Section III presents the design of a THz antenna element. In Section IV, comparisons of different full-wave models of the antenna array are discussed. The array expansion to 4×4 elements, simulation results, and comparisons with other works are presented in Section V. Section VI describes the manufacturing steps of the proposed antenna. Measurement results

compared to simulated ones and surface roughness measurements with recommendations for manufacturing steps are given in Section VII. The results of the proposed antennas and studies are concluded in Section VIII.

II. MODELING METAL AT THZ FREQUENCIES

At lower frequencies, the electromagnetic field can be assumed to rapidly decay in metal, and the metallic surface can be approximated by a perfect electric conductor with a relatively small deviation from reality as the metal thickness is still large enough compared to the skin depth (skin depth value at 1 GHz: for copper $\delta_{cu} = 2.09\ \mu$m, for gold $\delta = 2.37\ \mu$m). At terahertz frequencies, the behavior of metals significantly changes since several factors can affect metal conductivity, at a thinner metal thickness especially. This, in turn, decreases the metal skin depth and makes it comparable to the metal thickness at such frequencies. Hence, the approximation of the metal as a perfect electric conductor is not valid anymore and different effects have to be taken into consideration in the numerical modeling of metal surfaces.

The conductivity of a bulky gold varies from 41 MS/m to 45 MS/m typically. In [23], the conductivity of thin films of gold was shown to decrease when the film gets thinner and the frequency gets higher. At 1 THz, the conductivity reaches 7.5 MS/m for a 7 nm thick film of gold; such a film thickness is significantly lower than the skin depth.

For the proper modeling of different structures with thin gold layers at THz frequencies, the relationship between the thickness of the gold layer and the conductivity is discussed in detail. Test models were created in HFSS and CST Microwave Studio.

In case of the time-domain finite-integration technique (CST Microwave Studio), we have considered:

- Default options (no additional boundary conditions were associated with a thin gold layer).

In case of the frequency-domain finite-element technique (HFSS), different methods have been considered:

- Default options (no additional boundary conditions were associated with a thin gold layer),
- Meshing inside the gold layer,
- *Finite Conductivity* boundary was applied,
- *Layered Impedance* boundary was associated.

In addition to the two main models including the default modeling in CST and HFSS simulators, three other models were tested.

First, HFSS with solving fields inside the metal layer was used. This method is usually used for metals with low conductivities (lower than 0.1 MS/m). Exploiting this method forces the simulator to mesh with the utilization of tetrahedral structures and to compute the fields, even inside the conductor, for more accurate results. However, this approach subsequently increases the complexity of simulations due to a larger mesh.

The next method is using a finite conductivity boundary condition for the metal layer, which is a method proposed for imperfect conductors. While simulating a perfect electric conductor, all tangential electric field components are ignored. In the finite conductivity method, these components are estimated using

$$E_{tan} = Z_s \left(\hat{n} \times H_{tan}\right) \tag{1}$$

where E_{tan} and H_{tan} are the tangential components of the electric and magnetic fields respectively, $\hat{n}$ is the unit normal vector of the layer, and Z_s is the surface impedance of the boundary. Z_s can be calculated as

$$Z_s = (1 + j)/(\delta\sigma) \tag{2}$$

where δ is the skin depth and σ is the conductivity of the conductor. It is worth to mention here, that the finite conductivity boundary only approximates the behavior of the field at the surfaces of the metal without the actual calculation of fields inside it as in the previous method.

Finally, the last method – the layered impedance – consists of modeling the problem as a set of multiple layers starting from the first vacuum-material boundary onwards. HFSS estimates the tangential electric field components in the same way as in the previous method (1) except that it calculates the impedance of the surface, based on the material properties and metal thickness as

$$Z_s^i = Z^i \frac{Z_{tran}^i}{Z^i \cosh(\gamma_i T_i) + Z_s^{i+1} \sinh(\gamma_i T_i)} \tag{3}$$

where γ_i is the transverse propagation constant of the i$^{\text{th}}$ layer which has a thickness of T_i. γ_i is calculated as

$$\gamma_i = k_0 \sqrt{\mu_r^i \varepsilon_{cr}^i} \tag{4}$$

where ε_{cr}^i and μ_r^i are the relative complex permittivity and permeability for the i$^{\text{th}}$, which are calculated as follows:

$$\varepsilon_{cr}^i = \varepsilon_r^i - j\left(\frac{\sigma^i}{2\pi f_r \varepsilon_0} + \varepsilon_r^i tan\delta_\varepsilon\right) \tag{5}$$

$$\mu_{cr}^i = \mu_r^i - j\left(\mu_r^i tan\delta_\mu\right) \tag{6}$$

Z^i and Z_{tran}^i are the intrinsic and the transfer impedances of layer i$^{\text{th}}$ calculated as

$$Z^i = \sqrt{\left(\mu_0 \mu_r^i\right) / \left(\varepsilon_0 \varepsilon_{cr}^i\right)} \tag{7}$$

$$Z_{tran}^i = Z^i \sinh(\gamma_i T_i) + Z_s^{i+1} \cosh(\gamma_i T_i) \tag{8}$$

If this metal is an internal layer, the surface impedance in (2) will be equal to the average impedance estimated for both sides of the metal layer which are in contact with the computational domains.

As a proof of concept for showing the effect of different simulation models, a metallic waveguide with an internal thin metal wall was studied. The used waveguide was WR 2.2 with dimensions of 0.570 mm × 0.285 mm. WR 2.2 provides a single-mode TE_{10} performance at the frequency of interest (350 GHz). The waveguide was terminated by a wave port to act as a matched load. An internal thin metallic wall, with the

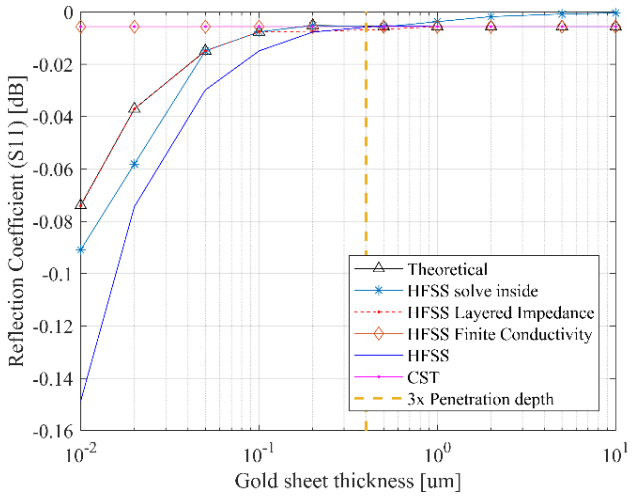

FIGURE 1. Reflection coefficient at the input port of waveguide as a function of gold wall thickness in the cross-section at 350 GHz.

same cross-section as the waveguide, was placed in the center of the waveguide. The thickness of the gold layer varied in a range from 0.01 μm to 10 μm. The gold has a skin depth $\delta = 0.132$ μm at the tested frequency of 350 GHz. The reflection coefficient at the terminal of the thin metallic wall was observed.

For comparison purposes, the theoretical calculations of the reflection coefficient were also performed following [24] as:

$$S_{11} = \frac{\left(Z_L^2 - Z_w^2\right) tan(\beta T)}{2Z_L Z_w + \left(Z_L^2 + Z_w^2\right) tan(\beta T)} e^{-j\beta L_w} \quad (9)$$

Here, β stands for the propagation constant of the gold layer and Z_w is the characteristic impedance of the waveguide (Z_{TE} in this case) which has a length of L_w.

In Fig. 1, the reflection coefficient at the input port of the waveguide at 350 GHz is depicted as a function of the gold-layer thickness using the previously discussed methods.

The default HFSS and CST simulators clearly deviate from the accurate performance in case of the metal thickness smaller than the skin depth. This can provide a remarkable difference between simulations and measurements for THz arrays if the designers did not consider this point in their calculations. Even, finite conductivity boundary condition which is used for imperfect conductor does not provide good results for such cases, unless the conductor starts to be thick enough (metal thickness above the double of its skin depth). On the other hand, HFSS simulations with a layered impedance boundary condition and with solving inside agree well with the theoretical values. For thicknesses much higher than the penetration depth, all the simulations start to convergence with similar values close to the theoretical ones.

Equivalent analyses done at frequencies 200 GHz and 500 GHz led to the same conclusions that acceptable outputs are obtained if the gold layer thickness is:

- Lower than 3δ (HFSS layered impedance or solve inside);
- Higher than 3δ (all expect HFSS with solving inside).

Considering these conclusions, conditions at the boundary of the gold and the air can be efficiently modeled depending on the operation frequency and the thickness of the gold layer.

The next section shows what way this approach can be applied when developing a CPU-time efficient numerical model of a terahertz antenna array.

III. DESIGN OF THE ANTENNA

The proposed THz antenna operates at $f_0 = 350$ GHz and is designed to allow the expansion into a larger antenna array. An antenna element consisting of 4 radiating slots is presented in Fig. 2. The antenna element consists of five layers with hollow, metalized slots, cavities and waveguides, all those layers have the same thickness t = 0.2 mm. The top layer is a dielectric layer with rotated metallic patches.

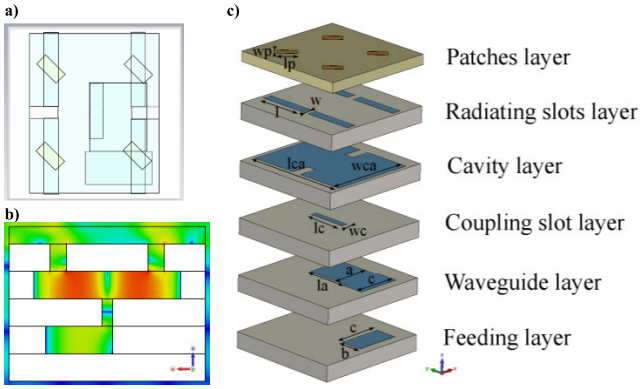

FIGURE 2. Designed terahertz antenna element, a) top view, b) Y-axis cut electric field distribution inside the antenna element c) antenna element design with layers names and parameters.

The signal is fed to the antenna element from the bottom of the feeding layer from a WR2.2 waveguide. The feeding layer and the waveguide layer create an E-bend transmission that has a transmission coefficient of -0.3 dB. The excitation method by slot coupling is applied here. The coupling slot is located on the top of the waveguide, longitudinally in the left corner. The signal from the waveguide is coupled to the cavity by the coupling slot, which is located centrally with respect to the cavity.

The simulated electric and magnetic field distribution in the air-filled cavity is shown in Figure 3. The central-plane of the cavity along the y-axis is equivalent to an electric wall. Therefore, the direction of the field in the right part of the cavity is opposite to the field in the left part of the cavity. Thanks to this, four slots can be excited not only with the same amplitude but also in-phase.

Four radiating slots are fed from the cavity equally. The position of the slots with respect to the cavity is defined by the element (slots) spacing which is 0.86 λ_0 for x and y-axis. Above the slots, the dielectric layer with metallic patches is located, and the patches are rotated by 45° with respect to the slots. The thickness of the dielectric layer (Arlon CuClad217) is $h = 0.127$ mm. The layer of patches is responsible for

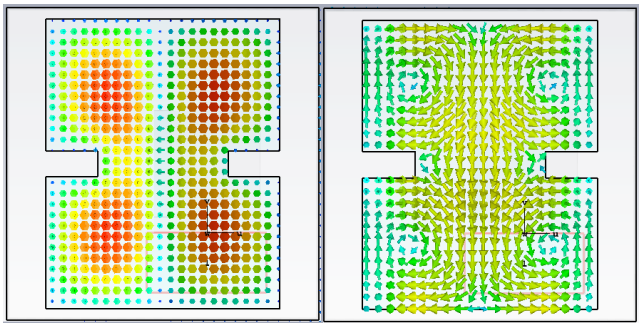

FIGURE 3. The electric (left) and magnetic (right) field distribution in the cavity of the antenna element.

TABLE 1. Dimensions used in the antenna design.

Name	Parameter	Value (mm)
Patch length	wp	0.24
Patch width	lp	0.11
Radiating slot length	l	0.63
Radiating slot width	w	0.12
Cavity length	lca	0.68
Cavity width	wca	0.55
Iris wall length		0.25
Iris wall width		0.11
Coupling slot length	lc	0.5
Coupling slot width	wc	0.08
Waveguide length	la	0.58
Waveguide width	a	0.5
E-bend waveguide width	c	0.57
Waveguide height	b	0.285
Layer thickness	t	0.2
Dielectric layer thickness	h	0.127

the creation of the circular polarization and improves the impedance matching [25].

The surface current on one of the patches in the layer of patches is shown in Figure 4. Obviously, the circular polarization is created on the patches because of the current changes its direction by 90° for every 90° phase change. The size of the antenna element (2 × 2 array) is $1.75\lambda_0 \times 1.75\lambda_0 \times 1.3\lambda_0$.

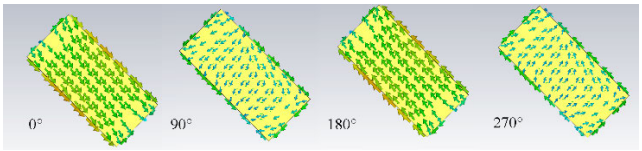

FIGURE 4. The surface current distribution on the patches in the top layer in phases: 0°, 90°, 180° and 270°.

The dimensions of the antenna elements are depicted in Fig. 2, the values of the dimensions are given in Table 1. The antenna element is designed to enable an easy expansion to a large array.

IV. MODELING OF TERAHERTZ ANTENNA

The in-depth analysis of a terahertz antenna array with thin metallic walls is costly in terms of computational resources needed. A simplified analysis is necessary for quick, preliminary antenna design, and can be useful during the optimization. To demonstrate potential simplifications, three models of the 2 × 2 array were created:

- The precise model of the antenna, accurately modeling the structure, serves here as a reference. Functional surfaces of the silicon ($\varepsilon_r = 11.64$, $\tan\delta = 0.001$ at 350 GHz [26]) were metalized by a 0.4 μm thick layer of gold.
- A full-gold model. The silicon below the gold layer was replaced by gold. Hence, the antenna was conceived as hollow waveguides and slots in the bulk gold.
- The PEC model. Gold in the full-gold model was replaced by a perfect electric conductor.

The models were analyzed in CST (time-domain finite-integration technique) and HFSS (frequency domain finite-element method).

Frequency responses of the magnitude of the reflection coefficient at the input port of the antenna array of different models are shown in Figure 5. PEC models and bulky-gold models result in very similar responses. The difference between CST and HFSS is given by different meshes. Whereas CST approximated the structure by 2.500.000 elements, HFSS used about 100.000 elements to represent the structure.

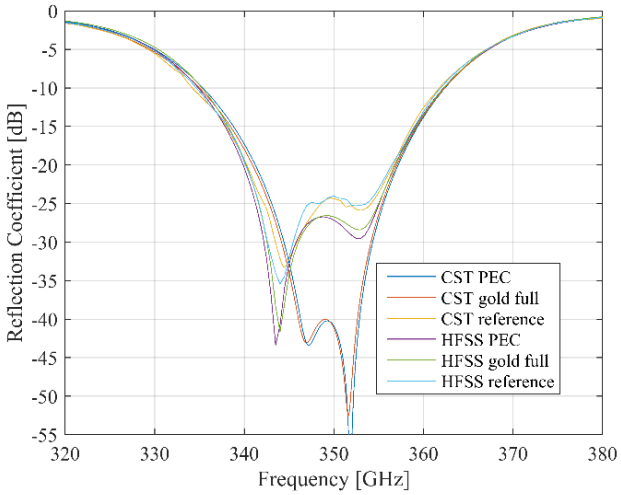

FIGURE 5. Frequency response of reflection coefficient at the input port of the antenna array: comparison of different models and solvers.

Reference models developed in CST and HFSS show a reasonable agreement. Whereas all the HFSS results are close to the reference, CST outputs for simplified (PEC and full-gold) models slightly deviate in the resonant frequency (352 GHz versus 346 GHz). On the other hand, the good matching (below −35 dB) and the bandwidths are almost identical.

Frequency responses of gain and axial ratio of the antenna array in the main lobe direction of the different models are shown in Figure 6. Since responses of the axial ratio and gain are in a close agreement for the bulky-gold model and the PEC one, the only line denoted PEC is used to represent both

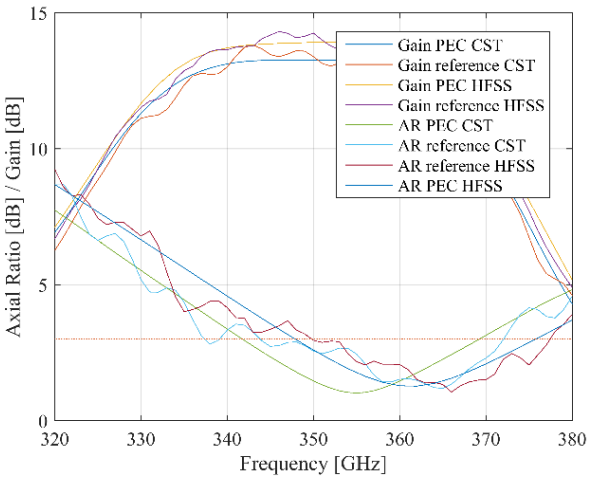

FIGURE 6. Frequency response of gain and axial ratio of the antenna array: comparison of different models and solvers.

TABLE 2. Numerical parameters of models.

Model	Cells [$\times 10^3$]	CPU time [hh:mm:ss]	Memory [GB]
CST PEC	2 500	00:02:41	1.1
CST bulky gold	2 500	00:02:53	1.2
CST reference	24 500	02:31:00	7.4
HFSS PEC	105	02:15:00	7.0
HFSS bulky gold	111	00:50:00	7.9
HFSS reference	131	03:45:00	8.3

the models. The gain response shows the realized gain for left-handed circular polarization.

Frequency responses of reference models exhibit deteriorations compared to smooth responses of simplified models. These deteriorations are related to the fact, that the whole outside surface of the antenna is metalized for the fully metallic models, while the outer surface consists mostly of silicon for the reference model. (the layers on the edges cannot be fully metalized during the) The lack of the metallization on the outer walls causes changes in radiation patterns, which is closely related to gain and axial ratio.

No matter there are minor discrepancies in the results, agreement between simplified and reference models is reasonable. Additionally, outputs of the HFSS simplified model are closer to precise models than CST ones.

The numerical parameters of compared models are summarized in Table 2. The CST reference model requires 10 times more mesh cells than simplified models; hence the computation time is increased from 2 minutes to more than 2 hours. In the case of HFSS models, the fastest analysis was achieved for the bulky-gold model (not the PEC one).

Table 2 shows that the CST PEC model shows the minimum CPU-time and memory demands. Hence, the CST-PEC model can be selected as a proper surrogate model for optimization. Considering the accuracy of results and the computation time, the HFSS bulky-gold model produces results agreeing well with the reference model. Nevertheless, CPU-time results are significantly lower compared to the reference model. For fine modeling, the HFSS bulky-gold model is recommended.

The PEC CST model is recommended to be used for fast and time-efficient calculations (a recommended choice for optimization). The antenna modeled this way can be fully characterized within the whole operating band in 2:41 minutes.

V. SIMULATION RESULTS AND COMPARISONS

The designed antenna element was simulated in CST Microwave Studio and achieved a peak of the realized gain for the left-handed circular polarization of 13.8 dBic.

The 2×2 antenna element was expanded to 4×4 array. The top layers were multiplied, and in the waveguide layer, a feeding system was introduced. This ensures an easy array expansion; only the feeding system needs to be designed.

The feeding system structure is presented in Figure 7. The feeding system consists of three waveguide-based T power dividers, which together make an H power divider structure. This structure is widely used and well described [27], [28]. The sizes of waveguides and the E-bend are the same as in the antenna element. To ensure equal power division, good isolation and reflection coefficient iris walls were placed in the middle of the three T dividers. The central iris wall has a size of 0.25 mm $\times$ 0.05 mm, while the left and right iris walls have a size of 0.30 mm $\times$ 0.05 mm.

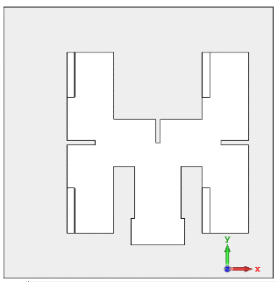

FIGURE 7. Feeding system, with three T-shaped power dividers, of the 4×4 antenna array.

The signal is feed to the antenna array through an E-bend transition located in the center bottom part of the H shaped feeding system. The feeding system has the reflection coefficient below -10 dB, the power splits to the four coupling slots equally with values -6.3 dB and the maximum deviation from this value is 0.04 dB.

In a similar manner, the array can be expanded to a very large number of elements, which enables this design to achieve outstanding gains. The 4×4 array achieves the simulated peak realized gain of the left-handed circular polarization of 18.4 dBic. The gain enhancement from 2×2 to 4×4 array is 4.6 dB.

The reflection coefficient and realized gain of the 4×4 and 2×2 antenna arrays vs. frequency are shown in Figure 8. The 2×2 antenna array operates in a frequency band of 27 GHz and the 4×4 antenna array in a frequency band of 30 GHz.

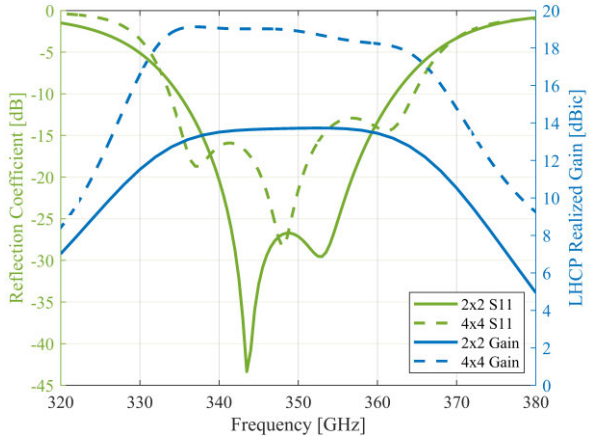

FIGURE 8. Simulated reflection coefficient and the left-handed circular polarization realized gain response vs frequency of the 2 × 2 and 4 × 4 antenna arrays.

Frequency bands are given for both impedance and polarization bandwidths.

The radiation efficiencies for both the 2 × 2 and the 4 × 4 antenna arrays are shown in Figure 9. In the operating band, the 2 × 2 antenna array has radiation efficiency above 0.9 and the 4 × 4 antenna array above 0.85. The presented efficiencies are given for the precise models that take into consideration all the metal and dielectric losses of materials. However, models do not account for manufacture inaccuracies (including over-etching and surface roughness). The efficiencies are expected to decrease for the fabricated antennas because of fabrication inaccuracies.

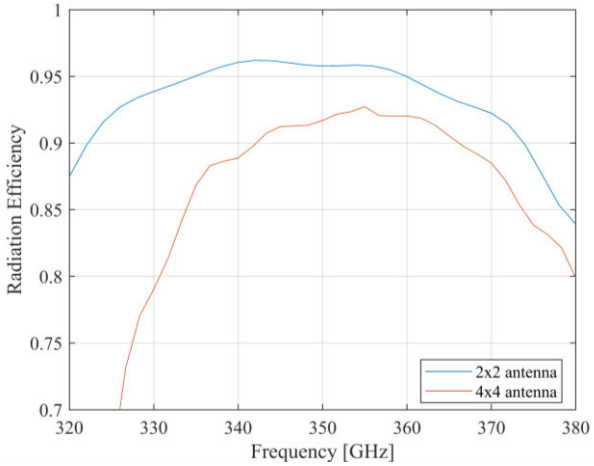

FIGURE 9. Simulated radiation efficiency of the 2 × 2 and 4 × 4 antenna arrays.

The radiation patterns of the 2 × 2 antenna element for phi = 0° and phi = 90°, for the right-handed and left-handed circular polarization, are depicted in Figure 10. The antenna shows a highly directive radiation pattern, with front to back ratio of 24 dB. The isolation between co-polar (LHCP) and cross-polar (RHCP) components at the boresight is higher than 35 dB. Radiation patterns for phi = 0° and phi = 90° for

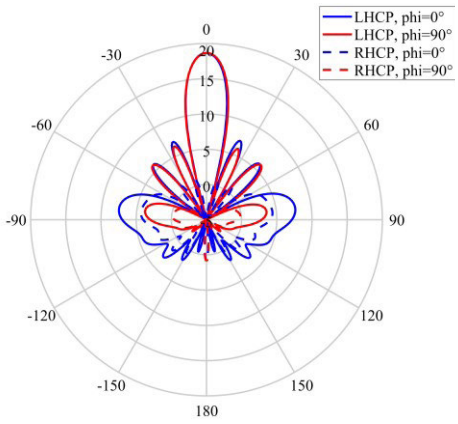

FIGURE 10. Simulated gain for phi = 0° and phi = 90° for the right-handed circular polarization (RHCP) and the left-handed circular polarization (LHCP).

the 4 × 4 antenna array at the bandwidth border frequencies (335 GHz and 365 GHz) and center frequency (350 GHz) for RHCP and LHCP are shown in Figure 11 and Figure 12.

To author's knowledge, the presented antenna design is the first design operating at 350 GHz with circular polarization, with wide impedance and polarization bandwidth and gain above 18 dBi that can be easily enlarged by a simple expansion of the array.

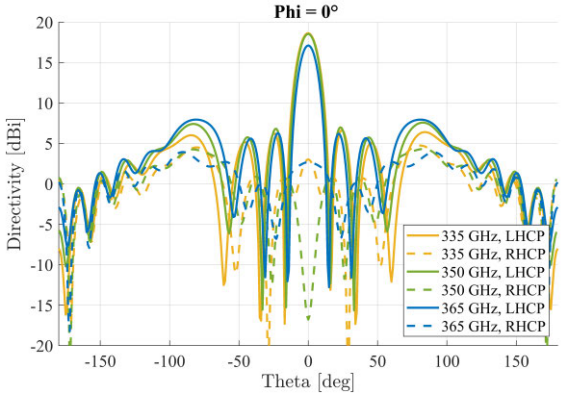

FIGURE 11. Directivity of the 4 × 4 antenna array for Phi = 0°.

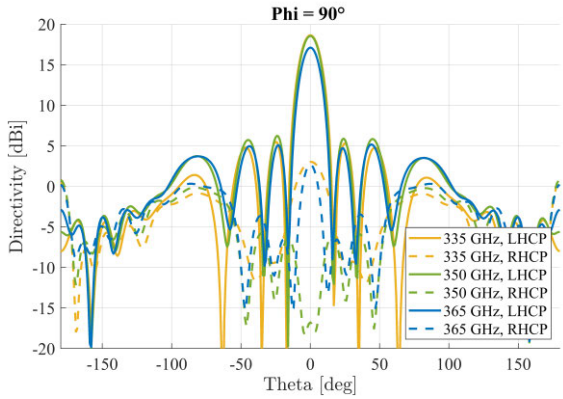

FIGURE 12. Directivity of the 4 × 4 antenna array for Phi = 90°.

TABLE 3. Comparison of high-gain/circularly polarized/THz frequency antennas with this work. Operation frequency f_c, impedance bandwidth BW, and circular polarization CP.

Ref.	Design	f_c (GHz)	Height (λ_0)	Size (λ_0)	BW (%)	Max gain (dBi)	CP
[1]	Bow-tie	350	0.12	2.3	20	6	Y
[2]	Horn	340	8.4	4	12	20	N
[3]	Fabry-Perot	10	0.05	5.7	0.3	15	Y
[3]	Fabry-Perot	1000	0.006	4.2	1.4	12	Y
[5]	Fabry-Perot	15	0.85	9.9	2	19	Y
[7]	Conical spiral	8	4.5	5.7	150	10	Y
[9]	Dielectric Rod	61	4	4.1	2	15	Y
[8]	4 × 4 Lens	257	14	31.1	160	30	N
[11]	4 × 4 Dielectric Rod	92.5	20.6	4.3	38	23.5	N
[12]	Dielectric Rod	155	11	0.76	19	17.5	N
[13]	4 × 4 Metallic posts array	1000	3	2.8	26	14	N
[14]	16 × 16 Slot array	350	7	18.1	13	30	N
[15]	16 × 16 Slot array	61.5	2	21.5	4	33	Y
This work	2 × 2 Slot array	350	1.3	2.5	8	13.8	Y
This work	4 × 4 Slot array	350	1.3	5	9	18.4	Y

In Table 3, comparison to other high-gain/circularly polarized antennas is given. The size is given as a diagonal in relation to λ_0. The bow-tie antenna presented in [1] operates with the circular polarization and in a wide band, however, has a gain of only 6 dBi. Horn antennas require a large height [2]. Fabry-Perot designs [3]–[5] provide circular polarization and comparable gains but have very narrow bandwidths, larger electrical sizes and operate only at lower frequencies. There is one design presented at THz [3], but it includes only simulations, was never fabricated and the manufacture constraints for THz frequencies were not considered.

Although dielectric rod array [6], lens array [4], corporate feed metallic posts array [13] and slots array [14] can achieve high gains and wide bandwidths, these antennas exhibit significantly larger heights and do not radiate with circular polarization.

Most of the antennas present interesting results, however, none of them achieve simultaneously high-gain, circular-polarization, wide bandwidth, low profile, and THz operation (feasibility of fabrication the design at THz frequencies).

VI. FABRICATION TECHNOLOGY

The analyzed antennas, 2 × 2 and 4 × 4 arrays, were manufactured following these technological steps:

- Structures (slots, cavities and waveguides) were cut by a laser in a p-type, 200 μm thick, 2-inch silicon wafer. The average accuracy of the cut structures was about 15 μm.
- Wafers were diced into 1 cm × 1 cm samples.
- The 400 nm thick gold layer was evaporated on the samples. The samples were tilted by 15° and rotating during the evaporation to ensure that gold covers surfaces inside the cavities and slots.
- Samples were bonded using silicon eutectic bonding, under 330° C and an average 100 N pressure on a FineTech Flip Chip machine. Bonding was performed layer by layer. Each process lasted 55 minutes.
- Copper patches on the top dielectric layer (Arlon CuClad217) were etched using a standard lithography process with a negative photoresist nLOF.
- A dielectric top layer was precisely aligned and glued to the antenna using the bonding machine without any heating.

The microfabrication steps are depicted in Figure 13.

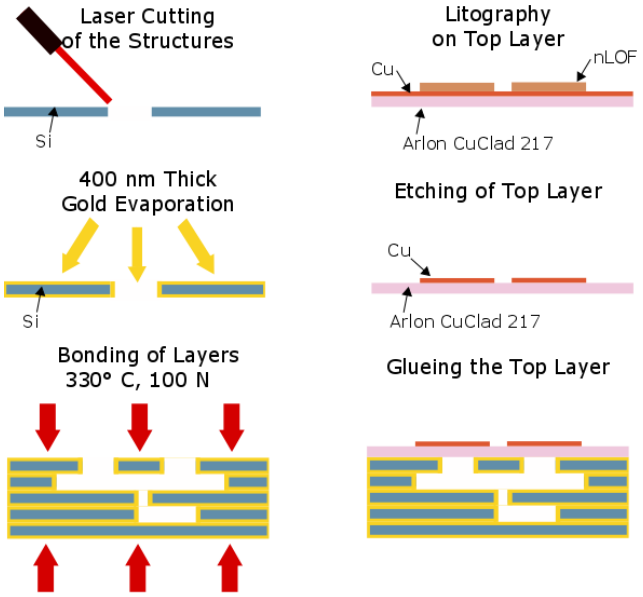

FIGURE 13. Microfabrication steps of the antennas.

The presented technology is much cheaper than microfabrication technologies used to fabricate similar antennas because deep reactive ion etching and vacuum bonding are not required. Instead, laser cutting and FineTech bonder were used which lowered the total cost of the antenna fabrication significantly. The manufactured 4 × 4 antenna array is shown in Figure 14.

VII. MEASUREMENT RESULTS

The 2 × 2 antenna array connected to the flange, which is used for coupling the signal from the VNA, is shown in Figure 15. In Figure 16, the measured reflection coefficients of two samples of the manufactured 2 × 2 antenna arrays and one 4 × 4 manufactured antenna array are presented, and the 2 × 2 simulation results are given for comparison. Deviations are due to manufacturing inaccuracies such as over-etching of the slots and cavities and high surface roughness, caused by laser cutting. Therefore, another simulation curve was added to the graph, taking manufacture inaccuracies into account (decreased conductivity, increased dielectric loss, dimensions of slots, and cavity varying within ±30 μm). The simulation with manufacture inaccuracies is similar to the measured results.

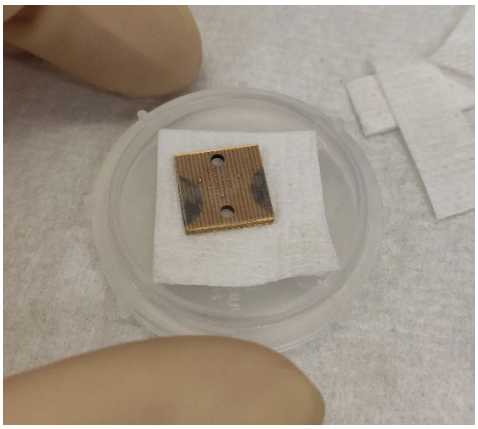

FIGURE 14. 4 × 4 antenna array before attaching to the flange.

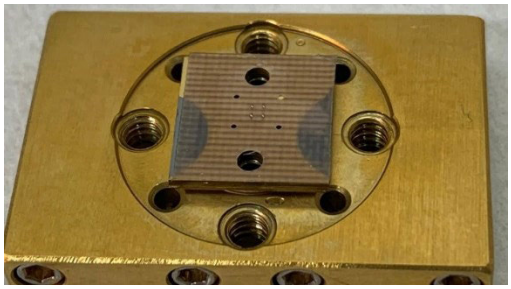

FIGURE 15. Manufactured 2 × 2 antenna array with dielectric top layer, stuck to a WR2.2 flange. The size of the antenna is 1 cm × 1 cm.

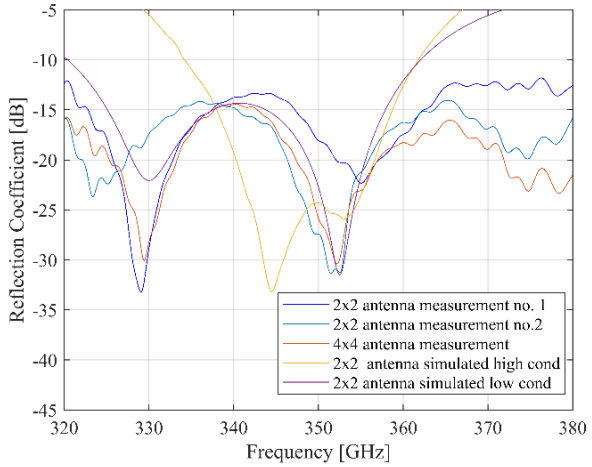

FIGURE 16. Measured frequency responses of the reflection coefficient compared with simulated ones.

Measurement of the radiation pattern was not performed because the necessary equipment was not available in our labs.

Surface roughness was measured by a scanning probe microscope. A picture of the scanned surface is presented in Figure 17. Black rectangles visible in the picture are due to the performed bonding and are elevated from the lighter color surface by around 1 μm.

The profile of the tested surface without the elevated black rectangles is presented in Figure 18. The average surface roughness (RMS) was calculated to be 500 nm which is higher than the gold layer thickness on the antenna surface.

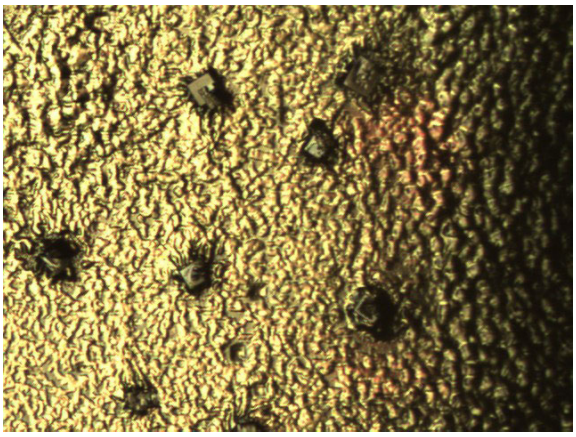

FIGURE 17. A photo of the surface tested for the surface roughness; the captured surface is roughly 200 μm × 250 μm.

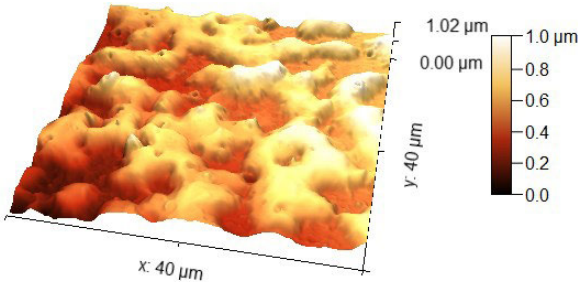

FIGURE 18. Surface roughness profile of 40 μm × 40 μm spot within the area presented in Figure 17.

Hence, the laser cutting increased the average value of the surface roughness to be high as the thickness of the antenna metal layer. This roughness decreased conductivity and introduced losses.

Moreover, the inaccuracy of the cutting changed the sizes of the slots and cavities resulting in changed resonance and coupling parameters. In the future manufacture of the antenna, the laser cutting will be avoided. Instead, a deep reactive ion etching will be used.

VIII. CONCLUSIONS

In the paper, the complete design of high-gain, low profile 2×2 antenna element slot antenna arrays with corporate feed is presented. The principle of feeding, radiation and creation of circular polarization is given. The 2×2 array is expanded to 4×4 array, the feeding system design is described. The antennas operate with circular polarization at 350 GHz, have polarization and impedance bandwidths wider than 27 GHz (8 %), with peak gains 13.8 dBic and 18.4 dBic, respectively.

The antenna performance is compared to other state-of-art designs. To author's knowledge, the presented design is the first antenna operating at THz frequency with simultaneously achieving such high gain, circular polarization, low-profile, wide bandwidth, and the possibility to extend to larger antenna arrays without significantly increasing the manufacturing/assembly complexity.

Moreover, we discuss the modeling of terahertz structures covered by thin metallic layers. For gold layers thinner than 3 δ, the default CST and HFSS approaches are not able to provide sufficiently accurate results. Hence, the recommended methods are layered impedance boundary conditions in HFSS and solving inside the metal in HFSS. The theory behind the methods is discussed in detail. The performance of different models of terahertz arrays was compared in terms of simulation time, memory consumption, and the number of mesh cells.

Finally, the manufacturing technology was described, and measurement results were shown. The presented microfabrication technology is cheaper and more available than the technologies presented so far. Three antenna arrays were manufactured and their performance was measured with VNA. Surface roughness was measured and included in the simulations to explain deviations from measurements.

REFERENCES

[1] A. Mir and J. Yu, "Broadband circular polarized cross bow tie antenna for terahertz range," in *Proc. IEEE Antennas Propag. Soc. Int. Symp. (APSURSI)*, Jul. 2014, pp. 416–417.

[2] C. Lee, G. Chattopadhyay, E. Decrossas, A. Peralta, I. Mehdi, C. A. Leal-Sevillano, M. A. Del Pino, and N. Llombart, "Terahertz antenna arrays with silicon micromachined-based microlens antenna and corrugated horns," in *Proc. Int. Workshop Antenna Technol. (iWAT)*, Mar. 2015, pp. 70–73.

[3] K. Pitra, Z. Raida, and J. Lacik, "Low-profile circularly polarized antenna exploiting Fabry–Perot resonator principle," *Radioengineering*, vol. 24, no. 4, pp. 898–905, Sep. 2015.

[4] B. A. Zeb and K. P. Esselle, "A partially reflecting surface with polarization conversion for circularly polarized antennas with high directivity," in *Proc. Int. Conf. Electromagn. Adv. Appl.*, Sep. 2012, pp. 466–469.

[5] R. Orr, G. Goussetis, and V. Fusco, "Design method for circularly polarized Fabry–Pérot cavity antennas," *IEEE Trans. Antennas Propag.*, vol. 62, no. 1, pp. 19–26, Jan. 2014.

[6] C. A. Balanis, *Modern Antenna Handbook*. Hoboken, NJ, USA: Wiley, 2008.

[7] K. A. Abdalmalak, G. S. Botello, S. Llorente-Romano, A. Rivera-Lavado, J. Flygare, J. A. L. Fernandez, J. M. S. Puente, L. E. Garcia-Castillo, D. Segovia-Vargas, M. Pantaleev, and L. E. Garcia-Munoz, "Ultrawideband conical log-spiral circularly polarized feed for radio astronomy," *IEEE Trans. Antennas Propag.*, vol. 68, no. 3, pp. 1995–2007, Mar. 2020.

[8] E. García-Muñoz, K. A. Abdalmalak, G. Santamaría, A. Rivera-Lavado, D. Segovia-Vargas, P. Castillo-Araníbar, F. Van Dijk, T. Nagatsuma, E. R. Brown, R. C. Guzman, H. Lamela, and G. Carpintero, "Photonic-based integrated sources and antenna arrays for broadband wireless links in terahertz communications," *Semicond. Sci. Technol.*, vol. 34, no. 5, 2019, Art. no. 54001.

[9] M. H. A. J. Rousstia, M. W., Herben, "Dual-circularly-polarized balanced-fed dielectric rod antenna for 60-GHz point-to-point wireless communication dual-circularly-polarized balanced-fed dielectric rod antenna for," in *Proc. URSI Benelux Forum*, 2013, pp. 1–3.

[10] A. Rivera-Lavado, L.-E. García-Muñoz, D. Lioubtchenko, S. Preu, K. A. Abdalmalak, G. Santamaría-Botello, D. Segovia-Vargas, and A. V. Räisänen, "Planar lens–based ultra-wideband dielectric rod waveguide antenna for tunable THz and sub-THz photomixer sources," *J. Infr., Millim., THz Waves*, vol. 40, no. 8, pp. 838–855, Aug. 2019.

[11] A. Rivera-Lavado, L.-E. García-Muñoz, A. Generalov, D. Lioubtchenko, K.-A. Abdalmalak, S. Llorente-Romano, A. García-Lampérez, D. Segovia-Vargas, and A. V. Räisänen, "Design of a dielectric rod waveguide antenna array for millimeter waves," *J. Infr., Millim., THz Waves*, vol. 38, no. 1, pp. 33–46, Jan. 2017.

[12] M. Geiger, M. Hitzler, and C. Waldschmidt, "A flexible dielectric leaky-wave antenna at 160 GHz," in *Proc. 47th Eur. Microw. Conf. (EuMC)*, Oct. 2017, pp. 240–243.

[13] K. M. Luk, S. F. Zhou, Y. J. Li, F. Wu, K. B. Ng, C. H. Chan, and S. W. Pang, "A microfabricated low-profile wideband antenna array for terahertz communications," *Sci. Rep.*, vol. 7, no. 1, pp. 1–11, Dec. 2017.

[14] K. Tekkouk, J. Hirokawa, K. Oogimoto, T. Nagatsuma, H. Seto, Y. Inoue, and M. Saito, "Corporate-feed slotted waveguide array antenna in the 350-GHz band by silicon process," *IEEE Trans. Antennas Propag.*, vol. 65, no. 1, pp. 217–225, Jan. 2017.

[15] J. Hirokawa, T. Tomura, Y. Miura, M. Zhang, and M. Ando, "Plate-laminated-waveguide corporate-feed slot array antennas with a polarization conversion layer," in *IEEE MTT-S Int. Microw. Symp. Dig.*, Sep. 2011, pp. 29–32.

[16] Y. Dong, P. Liu, D. Yu, B. Yi, and G. Li, "Active substrate integrated terahertz waveguide using periodic graphene stack," *AIP Adv.*, vol. 5, no. 11, pp. 1–7, 2015.

[17] P. C. Theofanopoulos and G. C. Trichopoulos, "Modeling of mmW and THz imaging systems using conjugate field coupling," *IEEE Antennas Wireless Propag. Lett.*, vol. 17, no. 2, pp. 213–216, Feb. 2018.

[18] R. Emadi, N. Barani, A. Amirhosseini, and R. Safian, "Hybrid analysis of terahertz photoconductive antennas using energy balance transport model," in *Proc. 40th Int. Conf. Infr., Millim., THz Waves (IRMMW-THz)*, Aug. 2015, pp. 1–2.

[19] Y. Zeng, T. Kreouzis, X. Chen, and R. S. Donnan, "Terahertz photoconductive antenna arrays—Analysis and optimization," in *Proc. IET Colloq. Millimetre-Wave THz Eng. Technol.*, Mar. 2015, pp. 4–6.

[20] J. Zhu, J. Bandler, N. Nikolova, and S. Koziel, "Antenna design through space mapping optimization," in *IEEE MTT-S Int. Microw. Symp. Dig.*, 2006, pp. 1605–1608.

[21] S. Pandey, B. Gupta, A. Chanana, and A. Nahata, "Non-drude like behaviour of metals in the terahertz spectral range," *Adv. Phys, X*, vol. 1, no. 2, pp. 176–193, Mar. 2016.

[22] N. Laman and D. Grischkowsky, "Terahertz conductivity of thin metal films," *Appl. Phys. Lett.*, vol. 93, no. 5, pp. 1–4, 2008.

[23] Y. Poo, R. X. Wu, X. Fan, J. Q. Xiao, and B. Bin Jin, "An experiment study of gold nano-film's conductivity at microwave and terahertz frequencies," in *Proc. Asia–Pacific Microw. Conf. APMC*, vol. 2, no. 1, Dec. 2010, pp. 1452–1454.

[24] A. Berenguer, M. Baquero-Escudero, D. Sanchez-Escuderos, and F. Vico, "Rigorous method for calculating gap waveguides impedance using transmission line theory," in *Proc. 8th Eur. Conf. Antennas Propag. (EuCAP)*, Apr. 2014, pp. 2508–2512.

[25] D. Warmowska and Z. Raida, "High-gain circularly polarized corporate-feed terahertz antenna array," in *Proc. Int. Conf. Electromagn. Adv. Appl. (ICEAA)*, Sep. 2018, pp. 157–160.

[26] P. H. Bolivar, M. Brucherseifer, J. G. Rivas, R. Gonzalo, I. Ederra, A. L. Reynolds, M. Holker, and P. de Maagt, "Measurement of the dielectric constant and loss tangent of high dielectric-constant materials at terahertz frequencies," *IEEE Trans. Microw. Theory Techn.*, vol. 51, no. 4, pp. 1062–1066, Apr. 2003.

[27] J. Joubert and S. R. Rengarajan, "Design of unequal H-plane waveguide power dividers for array applications," *Microw. J.*, vol. 40, no. 2, pp. 24–34, 1997.

[28] K. Sarhadi and M. Shahabadi, "Wideband substrate integrated waveguide power splitter with high isolation," *Microw., Antennas Propag.*, vol. 4, no. 7, pp. 817–821, Jul. 2010.

DOMINIKA WARMOWSKA was born in Poland. She received the master's degree in electronics and telecommunications from the Gdansk University of Technology, Poland. She is currently pursuing the Ph.D. degree with the Department of Radio Electronics, Brno University of Technology, Czech Republic.

In 2016, she joined the Applied Electromagnetics group, Brno University of Technology, as a Ph.D. Student. She is one of the Convergence of Electronics and Photonics Technologies for Enabling Terahertz Applications (CELTA) researchers, that aim to converged electronics and photonics co-design in its research components and systems for sensing, instrumentation, imaging, spectroscopy, and communications at THz frequencies. In 2019, she was with the Nanophotonics and Terahertz Technology Department, Darmstadt University of Technology. Her research interests include THz antennas design and modeling and micro- and nanofabrication technologies.

KERLOS ATIA ABDALMALAK (Graduate Student Member, IEEE) received the B.Sc. degree (Hons.) (ranked 2nd among the colleagues) in communication engineering from Aswan University, Egypt, in 2011, and the M.Sc. degree in multimedia and communication from the Carlos III University of Madrid, in 2015, where he is currently pursuing the Ph.D. degree with the Department of Signal Theory and Communications.

He joined the Department of Electrical Engineering, Aswan University, as a Teaching Assistant. He has authored/coauthored ten Journal Citation Ranking "JCR" journals (seven in the first quartile Q1 and two in the second quartile Q2 following Thomson Reuters), two invited papers, and 27 international conference papers. His technical interests include antennas and propagation, ultrawideband/multiband antennas, reflector/feed systems, radio astronomy receivers, base stations, 5G communications, THz technologies, whispering gallery mode resonators, and millimeter/submillimeter waves. He has participated in nine research projects financed by the Madrid Regional Ministry of Education, Ministry of Economy and Business, Huawei, and other private companies with a total fund exceeds two million Euros.

Mr. Abdalmalak served as a TPC member/peer reviewer in several JCR journals and international conferences, such as *Optics Express*, PIER, IJIM, ITCE, EuCAP, ICEECC, AsiaSim, and CIAP. He received the Erasmus Mundus GreenIT grant, in 2014, the Young Scientists' Award (2nd Prize) by URSI, Spain, in 2017, and selected as the IEEE Ambassador for the IEEEXtreme 14.0 Competition at Region 8 (Europe, Middle East, and Africa), in 2020.

LUIS ENRIQUE GARCÍA MUÑOZ is currently a Full Professor at the Universidad Carlos III de Madrid, Spain. He has managed or participated in several national and European research projects on areas, such as antennas and array design. He has coauthored 63 articles in international journals and holds four patents. His current research interests include mm and sub-mm antennas, arrays, and radio astronomy instrumentation.

ZBYNEK RAIDA (Senior Member, IEEE) received the Communication Engineering Degree from the Faculty of Electrical Engineering and Communication (FEEC), Brno University of Technology, Brno, Czech Republic.

He has been with the Department of Radio Electronics, FEEC, since 1993, where he is currently a Professor. From 1996 to 1997, he was with the Laboratoire de Hyperfréquences, Université Catholique de Louvain, Louvain-la-Neuve, Belgium, where he was involved in variational methods of numerical analysis of electromagnetic structures. He has also been involved in numerical modeling and optimization of electromagnetic structures, exploitation of artificial neural networks for solving electromagnetic issues, and the design of antennas. He is a member of the IEEE MTT Society.